Volume 143 | Number 12 | 21 June 2018 | Pages 2707–2924

Analyst

rsc.li/analyst

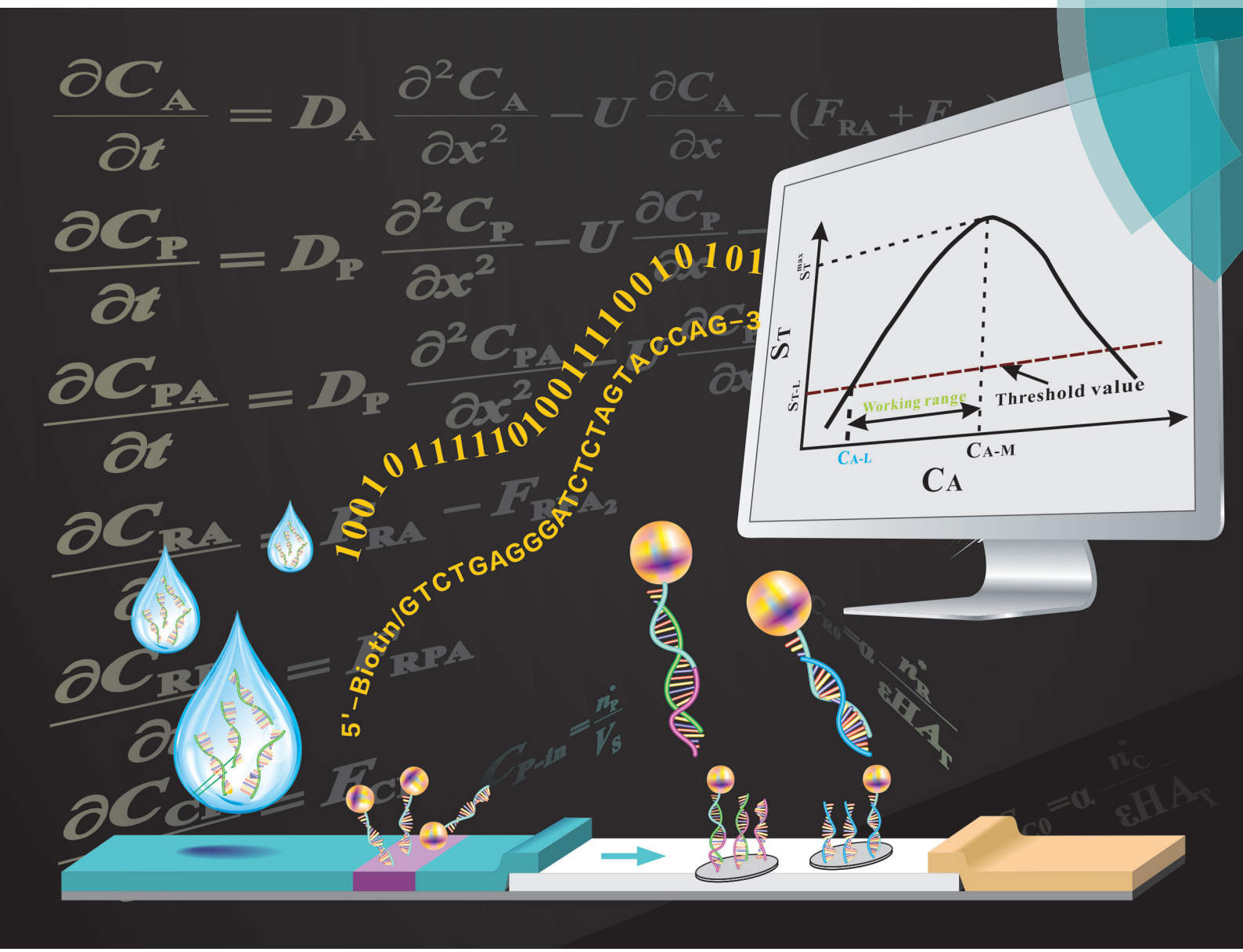

ISSN 0003-2654

ROYAL SOCIETY OF CHEMISTRY

PAPER
Zhiguo Qu, Feng Xu *et al.*
An improved detection limit and working range of lateral flow assays based on a mathematical model

Analyst

PAPER

Cite this: *Analyst*, 2018, **143**, 2775

An improved detection limit and working range of lateral flow assays based on a mathematical model

Zhi Liu,[a,b] Zhiguo Qu, *[a] Ruihua Tang,[c,d] Xiaocong He,[b,c] Hui Yang,[e] Dan Bai[c,f] and Feng Xu *[b,c]

Received 30th January 2018,
Accepted 15th April 2018

DOI: 10.1039/c8an00179k

rsc.li/analyst

Lateral flow assays (LFAs) have attracted considerable attention in biomedical diagnostics. However, it's still challenging to achieve a high detection sensitivity and extensive working range, mainly because the underlying mechanism of complex reaction processes in LFAs remains unclear. Many mathematical models have been developed to analyze the complex reaction processes, which are only qualitative with limited guidance for LFA design. Now, a semi-quantitative convection-diffusion-reaction model is developed by considering the kinetics of renaturation of nucleic acids and the model is validated by our experiments. We established a method to convert the LFA design parameters between the simulation and experiment (*i.e.*, inlet reporter particle concentration, initial capture probe concentration, and association rate constant), with which we achieved a semi-quantitative comparison of the detection limit and working range between simulations and experiments. Based on our model, we have improved the detection sensitivity and working range by using high concentrations of the inlet reporter particles and initial capture probe. Besides, we also found that target nucleic acid sequences with a high association rate constant are beneficial to improve the LFA performance. The developed model can predict the detection limit and working range and would be helpful to optimize the design of LFAs.

1. Introduction

Lateral flow assays (LFAs), as a promising point-of-care testing (POCT) platform, have drawn considerable attention in various fields (*i.e.*, global and public health care, agriculture, food safety, and environment monitoring[1,2]) due to their cost-effective, rapid, convenient, and disposable features.[3,4] Conventional LFAs are still limited by their poor sensitivity[5,6] and narrow working range (WR)[7] despite their significant potential and advantages. To address these problems, various strategies have been developed to improve the detection sensitivity by controlling the liquid migration behavior (*i.e.*, architecture modification[8] and integration with other strips[9]) and to achieve semi-quantitative detection with a wide detection range by increasing the detection lines (*i.e.*, multi-detection line LFAs[10] and three-line LFAs[11]). However, it is still challenging to achieve high detection sensitivity and a wide working range, mainly because the underlying mechanism of complex reaction processes in LFAs remains unclear.

Recently, significant efforts have been put on experimentally investigating the effects of the design parameters in manipulating LFAs (*i.e.*, concentrations of the reporter particle and capture probe) on the LFA performance. For example, the detection signal intensity of LFAs has been found to increase with the increase of reporter particle concentration, but remains unchanged with a further increase of reporter particle concentration when the capture capacity of the capture probe in the test line is saturated.[12] In addition, the capture probe concentration in the test line plays a crucial role in LFA performance.[13] The color intensity presents an amplified tendency with the increasing concentration of the capture probe in the test line due to the strong capture capability of capture probes for target–AuNP complexes.[12,14] However, excess capture probes may induce an adverse effect on the detection signal of LFAs mainly because the excess of capture probes will occupy the available avidin–biotin-binding sites and their capture capability for free target will be reduced.[12] Despite these efforts, it is still challenging to fundamentally reveal the

[a]*Key Laboratory of Thermo-Fluid Science and Engineering of Ministry of Education, School of Energy and Power Engineering, Xi'an Jiaotong University, Xi'an 710049, P.R. China. E-mail: zgqu@mail.xjtu.edu.cn*
[b]*Bioinspired Engineering and Biomechanics Center (BEBC), Xi'an Jiaotong University, Xi'an 710049, P.R. China. E-mail: fengxu@mail.xjtu.edu.cn*
[c]*Key Laboratory of Biomedical Information Engineering of Ministry of Education, School of Life Science and Technology, Xi'an Jiaotong University, Xi'an 710049, P.R. China*
[d]*College of Bioresources Chemical and Materials Engineering, Shaanxi University of Science and Technology, Xian 710021, China*
[e]*School of Life Sciences, Northwestern Polytechnical University, Xi'an 710072, P.R. China*
[f]*Department of Biochemistry and Molecular Biology, School of Medicine, Xi'an Jiaotong University Xi'an, Shaanxi Province 710061, China*

underlying mechanism of LFA performance, mainly due to the limitations associated with experimental approaches, such as complexity in manipulation, loss of portability, and poor repeatability.

By contrast, mathematical models have provided a powerful tool to simulate dynamic characteristics and assess the effects of crucial design parameters in LFAs. For instance, the convection–diffusion–reaction (CDR) model was developed to qualitatively predict the performance of LFAs with competitive and sandwich formats.[15,16] This CDR model was later introduced to optimize the position of the test line and the sample volume in LFAs, which however was not validated by experimental results.[17] Recently, another modified CDR model was developed to investigate the effect of the binding site density on the reporter particle surface and the concentration of reporter particles on the performance of LFAs.[18] This study only provided a qualitative comparison with experiments to verify the simulation results. Furthermore, Zeng *et al.*[19,20] developed nonlinear state-space models to estimate the LFA performance without quantitative experimental comparison. In the existing models, the quantitative comparison with experiments is lacking because the main design parameters were determined through assumptions and not from experiments. Therefore, these models may produce a deviation in predicting the actual performance of LFAs and are not capable of predicting the detection limit and working range for a specific experiment. Therefore, there is still an unmet need for an effective model based on the experimental design parameters to reveal their effects on LFA detection for improved performance.

In the current study, we investigated the effects of design parameters (*i.e.*, inlet reporter particle, initial capture probe concentrations and association rate constant) on the performance of LFAs by using experimental and simulation methods. Our mathematical model considered the kinetics of renaturation of nucleic acids to calculate the association and dissociation rate constants. We also established an effective conversion method to obtain the inlet reporter particle and initial capture probe concentrations based on experimental parameters. Moreover, we investigated the detection limit and working range under different inlet reporter particle and initial capture probe concentrations and varying association rate constants with this model. The model was semi-quantitatively validated by direct comparison with experimental data. The fundamental research of influence factors on LFAs may aid in providing physically and synthetically intuitive guidance for the design of LFAs with a high sensitivity and wide working range.

2. Materials and methods

2.1 Experimental section

Preparation of AuNPs-detector probe (DP) conjugates, capture probe, and control probe. All oligonucleotide sequences used in the current study are purchased from Sangon Biotechnology Co., Ltd (Shanghai, China) (Table 1). AuNPs with a size of 13 ± 3 nm in diameter were used as the reporter particles in the experiments and prepared according to the previously established method.[21] Subsequently, AuNPs were decorated with HIV-DP to form AuNP-DP conjugates by following the reported protocol.[22] Then, 1 mL of the prepared AuNP-DP solution was used and filled into 1.5 ml of centrifuge tube for centrifugation. The supernatant and red pellets (gold nanoparticles) were separated after centrifugation at 145 000 rpm for 25 min. Then, the red pellets were redispersed in 100 μL of eluent buffer for LFA strips fabrication. Based on the calculation method of Shang and Gao,[23] the concentration of the as-prepared AuNP-DP (C_P^*) mainly depends on the Avogadro constant (N_A), the volume of AuNP-DP solution (V), the total weight of Au atoms (m_t), and the average weight of one gold nanoparticle (m_P). The pre-loaded concentration of AuNP-DP is expressed as,

$$C_P^* = \frac{m_t}{N_A \cdot V \cdot m_P}. \quad (1)$$

Thus, the concentration of the as-prepared AuNP-DP is calculated as 36.7 nM. Then, a series of AuNP-DP concentrations (*i.e.*, 18.35, 9.18, and 3.67 nM) are obtained by the gradient dilution method using the eluent buffer.

Table 1 Oligonucleotide sequences applied in the current study

Name	Sequence
HIV-detector probe	5′-CACAA CAGAC GGGCA CACAC TACT-(CH2)6-HS-3′
Capture probe	5′-Biotin/GTCTG AGGGA TCTCT AGTTA CCAG-3′
Control probe	5′-AGTAG TGTGT GCCCG TCTGT TGTG/Biotin-3′
Target nucleic acid	5′-AGTAG TGTGT GCCCG TCTGT TGTGT GACTC TGGTA ACTAG AGATC CCTCA GAC-3′
Control nucleic acid	5′-GCCTC AATAA AGCTT GCCTT GAGTG CTTGT GGAAA ATCTC TAGCA GTGGC GCC-3′

The preparation process of control and capture probes is presented as follows. A 100 μM control probe was achieved by adding 13 μL of PBS and 67 μL of 2 mg mL^{-1} streptavidin into the control probe dry powder with 1 hour incubating time. Then, the incubated solution was added into 9 μL of ethanol for further use. Similarly, a 100 μM capture probe was achieved by adding 11 μL of PBS, 66 μL of 2 mg mL^{-1} streptavidin, and 9 μL of ethanol into the capture probe dry powder with a 1 hour interval. A series of capture probe concentrations (*i.e.*, 50, 25, and 10 μM) are obtained by diluting the abovementioned capture probe solution using the buffer solution with a fixed ratio of PBS and ethanol to optimize the capture probe concentration.

Fabrication of lateral flow test strips. LFA strips are fabricated by following the protocol from the previous study,[24] as shown in Fig. 1. In summary, the entire LFA strip is assembled by the immersing pad (1.9 cm length), absorbent pad (2.5 cm length), nitrocellulose (NC) membrane (2.0 cm length), and backing pad (6.0 cm length). Then, the LFA strip is cut into 3.0 mm width by using Matrix™ 2360 Programmable Sheer (Fig. 1a). Subsequently, 8 μL of AuNPs-DP conjugates (V_P^*) are encapsulated in the immersing pad with a 3 mm interval from the NC membrane. Afterward, 0.5 μL of control and capture

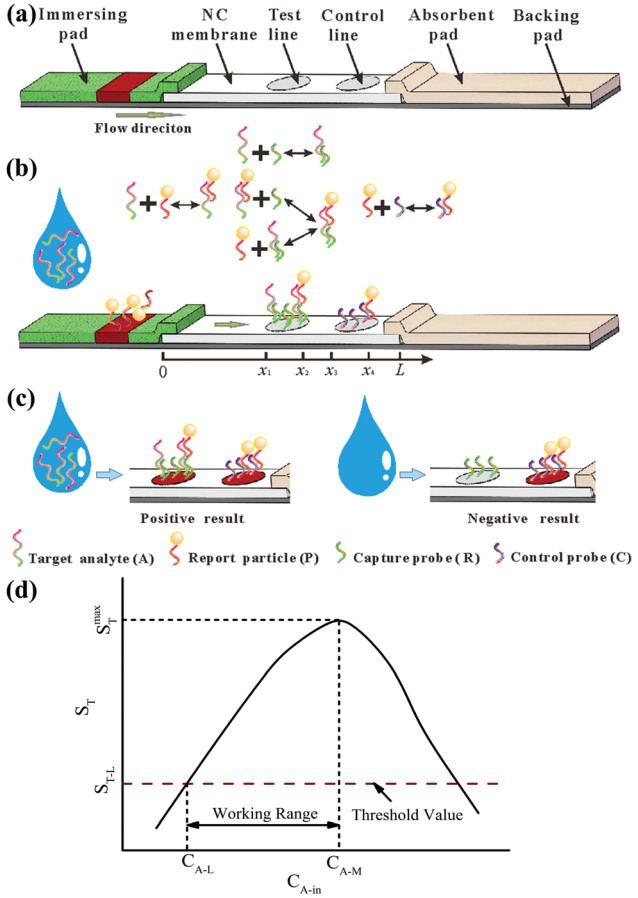

Fig. 1 Schematic illustration of LFAs. (a) Schematic of the configuration of LFAs; (b) schematic of the mathematical model; (c) illustration of detection results; (d) data processing.

probes (V_C^* and V_R^*) are immobilized on the NC membrane as control and test lines. As shown in Fig. 1b, the length L, thickness H, and porosity ε of the NC membrane are measured to be 20.0 mm, 0.13 mm, and 0.6, respectively. The test line-immobilized capture probe starts from x_1 to x_2 (x_1 = 0.5 L, x_2 = 0.65 L), whereas the control line-immobilized control probe starts from x_3 to x_4 (x_3 = 0.75 L, x_4 = 0.9 L). Therefore, the two wetting areas of the test line A_T and the control line A_C are equal to 7.1 mm^2. The total amount of AuNPs-DP conjugates n_P^* is equal to the product of C_P^* and V_P^* (*i.e.*, 293.6, 148.6, 73.44, and 29.36 fmol). Similarly, we can also calculate the total amount of the control probe n_C^* (*i.e.*, 50 pmol) and the capture probe n_R^* (*i.e.*, 50.0, 25.0, 12.5, and 5.0 pmol). Finally, all of the prepared LFA strips are placed in an oven at 37 °C for 2 hours to dry and then stored at room temperature for further use. In a group of experiments, different concentrations of target HIV nucleic acid (C_A^* = 5000, 1000, 500, 300, 200, 100, 50, 10, 5, 1, 0.5, 0.25, 0.1, 0.05, and 0 nM) were used to optimize the assay.

2.2 Mathematical model and formulation

Description of the physical process of LFA detection. The schematic of a typical sandwich format LFA strip is presented in Fig. 1b. LFAs use reporter particles as a chromogenic label to indicate the amount of target analytes combined with capture probes (previously immobilized in the test line). After the solution with HIV target analytes is added to the immersing pad, the solution flowed toward the absorbent pad driven by capillary action and the chemical reaction starts to occur. First, free analytes (A) will combine with the dissolved reporter particles (P) to form the complex reporter particle–analyte (PA). Subsequently, two methods are used to form the sandwich type of the complex capture probe–analyte reporter particle (RPA). First, the free A and PA will be captured by the capture probe (R) to form the complex capture probe–analyte (RA) and the complex RPA_1 (subscript "1" represents the first method to form complex RPA) when the solution passes through the test line. In addition, the free P can also be captured by RA to form RPA_2 (subscript "2" represents the first method to form complex RPA). After the liquid passes through the control line, control probe C will capture free P to form complex CP. A positive result is achieved when the concentration of HIV target analyte in the sample is above the detection limit, which is reflected by the appearance of the test and control lines (Fig. 1c). A negative result appeared only with the control line signal when the concentration of target HIV is below the detection limit. If no control line signal appears, then the assay fails probably due to invalid nucleic acids or inactivated reporter particles.

According to the first-order reversible reactions, the above interactions can be summarized as follows:

$$\mathrm{A} + \mathrm{P} \underset{k_{d1}}{\overset{k_{a1}}{\longleftrightarrow}} \mathrm{PA}, \tag{2a}$$

$$\mathrm{R} + \mathrm{A} \underset{k_{d2}}{\overset{k_{a2}}{\longleftrightarrow}} \mathrm{RA}, \tag{2b}$$

$$\mathrm{R} + \mathrm{PA} \underset{k_{d3}}{\overset{k_{a3}}{\longleftrightarrow}} \mathrm{RPA_1}, \tag{2c}$$

$$\mathrm{RA} + \mathrm{P} \underset{k_{d4}}{\overset{k_{a4}}{\longleftrightarrow}} \mathrm{RPA_2}, \tag{2d}$$

$$\mathrm{C} + \mathrm{P} \underset{k_{d5}}{\overset{k_{a5}}{\longleftrightarrow}} \mathrm{CP}. \tag{2e}$$

where k_{a1}, k_{a2}, k_{a3}, k_{a4}, k_{a5} and k_{d1}, k_{d2}, k_{d3}, k_{d4}, and k_{d5} are the association rate constants and dissociation rate constants for each reaction equation, respectively. Based on the kinetics of renaturation of nucleic acids in the research of Wetmur,[25] the association rate constant (k_a) for hybridization reactions could be determined by the following equation:

$$k_a = k'_N \frac{L_S^{1/2}}{N}. \tag{3}$$

where L_S is the length of the shortest strand participating in duplex formation, and N is the complexity or the total number of DNA base pairs present in non-repeating sequences. The values of L_S and N are the same for eqn (2a)–(2e) according to the nucleic acid sequences in Table 1. L_S and N are equal to 24 and 53, respectively. The nucleation rate constant k'_N is a func-

tion of ionic strength at salt concentrations[26] and can be expressed as follows:

$$k'_N = (4.35 \cdot \log_{10}[Na^+] + 3.5) \times 10^5 \quad \text{for } 0.2 \le [Na^+] \le 4.0. \tag{4}$$

where k'_N remains constant for eqn (2a)–(2e) according to the same reaction system. Therefore, k_{a1}, k_{a2}, k_{a3}, k_{a4}, and k_{a5} are equal due to the same reaction conditions (*i.e.*, fixed k'_N, L_S, and N). For simplification, the association rate constant can be uniformly described as k_a and can be calculated as 1.0×10^{-5} (nM^{-1} s^{-1}) based on previous experimental parameters. By contrast, the dissociation rate constant (k_d) is conservatively determined as a constant for the preceding reactions in accordance with the theoretical analysis and evaluation of Shkolnikov.[27] Therefore, k_{d1}, k_{d2}, k_{d3}, k_{d4}, and k_{d5} are equal and can described with k_d equal to 10^{-7} ($1\ s^{-1}$).

Mathematical and simulation model. We developed the CDR LFA model by considering the kinetics of renaturation of nucleic acids and established a conversion relationship between the simulation and experiment design parameters (*i.e.*, concentrations of reporter particles and capture probe) to investigate the underlying mechanism of physical phenomena in LFAs. Several assumptions have been made to conveniently establish the mathematical model. The NC membrane is considered to be the main calculation domain (from $x = 0$ to $x = L$ in Fig. 1b). At the initial moment, the target HIV and reporter particle are dissolved in the sample solution without participating in any reactions. The wetting behavior is driven by the capillary action with a constant and creeping velocity. The capture and control probes are uniformly distributed and fully wetted the detection and control lines.

According to the mass conservation principle, the governing equations are developed to describe the processes of fluid convection, particle diffusion, and reagent reaction in LFA detection. Moreover, the governing equations elucidate the balance between the changing rate of reagent concentration and the total changing rates of reagent concentration in diffusion, convection, and source terms. Thus, the concentration-governing equations of free A, PA, and RPA are depicted as follows:

$$\frac{\partial C_A}{\partial t} = D_A \frac{\partial^2 C_A}{\partial x^2} - U\frac{\partial C_A}{\partial x} - (F_{RA} + F_{PA}). \tag{5}$$

$$\frac{\partial C_P}{\partial t} = D_P \frac{\partial^2 C_P}{\partial x^2} - U\frac{\partial C_P}{\partial x} - (F_{PA} + F_{RPA_2} + F_{CP}). \tag{6}$$

$$\frac{\partial C_{PA}}{\partial t} = D_P \frac{\partial^2 C_{PA}}{\partial x^2} - U\frac{\partial C_{PA}}{\partial x} + F_{PA} - F_{RPA_1}. \tag{7}$$

The balance equations of the production rate of RA, RPA in the test line, and CP in the control line are written as

$$\frac{\partial C_{RA}}{\partial t} = F_{RA} - F_{RPA_2} \quad x_1 \le x \le x_2. \tag{8}$$

$$\frac{\partial C_{RPA}}{\partial t} = F_{RPA} \quad x_1 \le x \le x_2. \tag{9}$$

$$\frac{\partial C_{CP}}{\partial t} = F_{CP} \quad x_3 \le x \le x_4. \tag{10}$$

where C_A, C_P, C_{PA}, C_{RA}, C_{RPA}, and C_{CP} are the concentrations of free A, P, and the complexes PA, RA, RPA, and CP, respectively. The liquid wicking velocity U is experimentally measured to be 0.2 mm s^{-1}. Based on the Stokes–Einstein equation,[28] the diffusion coefficient D_A of free A is estimated to be 1.0×10^{-10} m^2 s^{-1}. Accordingly, the diffusion coefficients D_P of free P and the complex PA are estimated to be 1.0×10^{-12} m^2 s^{-1}.

In the governing equations, the source terms directly depend on the concentration production rates F_{PA}, F_{RA}, F_{RPA1}, F_{RPA2}, and F_{CP} of the complexes PA, RA, RPA, and CP in eqn (2a)–(2e), respectively. According to the mechanism of chemical kinetics, the production rates F_{PA}, F_{RA}, F_{RPA1}, F_{RPA2}, and F_{CP} corresponding to eqn (2a)–(2e) are respectively given as follows:

$$F_{PA} = k_a \cdot C_A \cdot C_P - k_d \cdot C_{PA}, \tag{11a}$$

$$F_{RA} = k_a \cdot (C_{R0} - C_{RA} - C_{RPA}) \cdot C_A - k_d \cdot C_{RA}, \tag{11b}$$

$$F_{RPA1} = k_a \cdot (C_{R0} - C_{RA} - C_{RPA}) \cdot C_{PA} - k_d \cdot C_{RPA}, \tag{11c}$$

$$F_{RPA2} = k_a \cdot C_{RA} \cdot C_P - k_d \cdot C_{RPA}, \tag{11d}$$

$$F_{CP} = k_a \cdot (C_{C0} - C_{CP}) \cdot C_P - k_d \cdot C_{CP}. \tag{11e}$$

where C_{R0} and C_{C0} are the initial concentrations of the capture probe in the test line and the control probe in the control line, respectively. Furthermore, the total production rate of complex RPA produced by the two methods shown in eqn (11c) and (11d) is given as:

$$F_{RPA} = F_{RPA1} + F_{RPA2}. \tag{12}$$

Initial and boundary conditions. At the initial moment, no sample solution reached the NC membrane. Thus, the initial condition is expressed in eqn (13),

$$C_A = C_P = C_{PA} = C_{RA} = C_{RPA} = C_{CP} = 0 \text{ at } t = 0. \tag{13}$$

Based on the previous assumptions, the sample with target HIV and reporter particle is in contact with the left side of the NC membrane. The expressions of left inlet boundary conditions are shown in eqn (14).

$$C_A = C_{A\text{-in}}, C_P = C_{P\text{-in}}, C_{PA} = 0 \text{ at } x = 0. \tag{14}$$

The outlet on the right side is considered to be fully developed conditions and expressed as follows:

$$\partial C_A/\partial x = 0, \partial C_P/\partial x = 0, \partial C_{PA}/\partial x = 0 \text{ at } x = L. \tag{15}$$

In eqn (14), $C_{A\text{-in}}$ and $C_{P\text{-in}}$ are the inlet concentrations of target HIV and reporter particle, respectively, in the sample solution. Based on the previous assumption, the inlet concentration of target HIV $C_{A\text{-in}}$ is equal to the experimental C_A^* ($C_{A\text{-in}}$ = 5000, 1000, 500, 300, 200, 100, 50, 10, 5, 1, 0.5, 0.25, 0.1, 0.05, and 0 nM). The inlet reporter particle was assumed

to be dissolved in the sample solution (V_S = 80 μL), and its corresponding concentration is expressed as follows:

$$C_{P\text{-in}} = \frac{n_P^*}{V_S}. \quad (16)$$

Correspondingly, the inlet reporter particle concentration $C_{P\text{-in}}$ in the simulation is calculated as 3.67, 1.853, 0.918, and 0.367 nM for four different cases. Therefore, we established a connection to effectively convert the experimental operation parameters into the corresponding simulation parameters (*i.e.*, $C_{A\text{-in}}$ and $C_{P\text{-in}}$).

Considering that the initial concentrations of the capture probe in the test line C_{R0} and the control probe in the control line C_{C0} are required to be known preferentially to the simulation, an effective conversion method should be established to obtain such concentrations from experimental operations. Initially, the capture and control probes were dried and stored in the NC membrane, which are then dissolved as the liquid passed through the testing process. The concentrations of rewetting capture and control probes were determined by the ratio between the total amount of moles and the effective volume of the test and control lines, respectively. However, determining the effective volume of the test and control lines is difficult due to the uncertain boundary location of the volume occupied by the capture and control probes in the porous structure. Thus, we assumed that the volume of the test and control lines is determined by the product of the porosity (ε), the thickness of the NC membrane (H), and the wetting surface of the capture probe A_T and control probe A_C in preparing LFA strips (Fig. 1a).

In addition, the capture and control probes cannot be completely immobilized on the NC membrane due to the limited link efficiency of streptavidin. The probes that are not immobilized on the NC membrane will be driven by the flowing liquid and are invaluable to the detection signal. Hence, the concentrations of capture and control probes will be overestimated, thus probably resulting in a discordance in the comparison between the simulation and experimental results. The immobilization efficiency can be defined to represent the ratio between the immobilized probes and the total amount of added probes in the experiments. The immobilization efficiency of the capture and control probes is extremely low and estimated to be approximately 10% on the surface of the gold substrate, as indicated by Peterson *et al.*[29] In the present study, the NC membrane, which has a porous and complicated structure, has strong repulsive electrostatic force and large steric hindrance. These characteristics will more seriously decrease the immobilization efficiency according to the research of Wang *et al.*[30] than that of the gold substrate. Therefore, the immobilization efficiency α was assumed to be 1% in the current simulation. Thus, the initial concentrations of the capture and control probes in the NC membrane can be written as follows:

$$C_{R0} = \alpha \frac{n_R^*}{\varepsilon \cdot H \cdot A_T}, \quad C_{C0} = \alpha \frac{n_C^*}{\varepsilon \cdot H \cdot A_T}. \quad (17)$$

The series of capture probe concentrations C_{R0} in the simulation can be calculated as 1068, 804, 402, and 160.8 nM based on the five preceding n_R^* mentioned in the experiments. In addition, the concentration of the control probe C_{C0} in the simulation can be calculated as 1068 nM based on the preceding n_C^* mentioned in the experiments.

Solution methods. The preceding governing equations and boundary conditions are discretized in uniform grid spacing using the finite difference method and are solved by using the three-diagonal matrix algorithms (TDMAs).[31] The solution procedure is similar to our previous paper,[18] which will not be described in detail here. Since the mathematical model is unsteady, we determined an equilibrium time (600 s) for the signal acquisition when the mathematical system reached stability.

Parameter definition. The effective signal in the test line is positively proportional to the total concentration of accumulated RPA in the test line. In addition, the effective signal in the control line is a proportional function of the total concentration of complex CP in the control line. Therefore, we calculate the average concentrations of RPA and CP to represent the detection signal in the test and control lines, respectively. The average concentration of RPA (S_T) in the test line is the integration of local RPA concentration, and the formula is expressed in eqn (18) as follows:

$$S_T = \int_{x_1}^{x_2} C_{RPA} dx/(x_2 - x_1). \quad (18)$$

Similarly, the average concentration of CP (S_C) in the control line is expressed in eqn (19)

$$S_C = \int_{x_3}^{x_4} C_{CP} dx/(x_4 - x_3). \quad (19)$$

The detection signal in the test line can be observed by the naked eye only when the accumulation of reporter particles S_T reaches a certain value. We defined a threshold value $S_{T\text{-L}}$ to distinguish the visible signal and invisible region (Fig. 1d) to characterize the simulation result. Thus, the detection limit ($C_{A\text{-L}}$) represents the lowest target analyte concentration corresponding to the threshold $S_{T\text{-L}}$.

We selected the peak target analyte concentration ($C_{A\text{-M}}$) corresponding to the maximum signal (S_T^{max}) as a reference value to define WR, which is the effective detection range from the detection limit ($C_{A\text{-L}}$) to the peak target analyte concentration $C_{A\text{-M}}$, namely

$$WR = \log(C_{A\text{-M}}) - \log(C_{A\text{-L}}). \quad (20)$$

3. Results and discussion

3.1 Performance of LFAs with different inlet reporter particle concentrations

Considering the importance of the inlet reporter particle concentrations, we first experimentally and numerically studied

the effects of the inlet reporter particle concentration on the performance of LFAs (Fig. 2). The experimental images show that S_T presents a similar tendency with the Hook effect for all four different inlet reporter particle concentrations (*i.e.*, $C_{P\text{-}in}$ = 3.67, 1.84, 0.918, and 0.367 nM), where it first increases to a peak value and then decreases with the increasing inlet concentration of target HIV (Fig. 2a). Additionally, a high inlet concentration of reporter particles applied in the fabrication of LFAs can improve the signal intensity in the test line.

For further quantitative analysis, the signal intensities (optical density) $S_{T\text{-}OD}$ from the experimental images are extracted by using the Image-Pro Plus 6.0 software. Although the exact corresponding relationship between the optical density and the amount of accumulated AuNPs in the test or control lines is not clearly established, the signal intensity is proportional to the amount of accumulated AuNPs in the test or control lines.[18] Thus, a semi-quantitative comparison between the optical density in the experiment and signal intensity in the simulation can be conducted in the present study. Then, we performed numerical simulations using different $C_{P\text{-}in}$ values (*i.e.*, 3.67, 1.84, 0.918, and 0.367 nM) to detect a series of $C_{A\text{-}in}$ and conduct a semi-quantitative comparison with the experimental results (Fig. 2b). Good agreement between S_T and $S_{T\text{-}OD}$ is observed for different $C_{P\text{-}in}$, which provides a reasonable validation for our model. We did not observe any signal in the test line at a low target concentration (Fig. 2b), because the concentration of the target in the sample is below the detection limit. Compared with the lowest detection limit of experiments, the threshold value for the simulation result is approximately determined as $S_{T\text{-}L}$ = 0.03 (nM) (the red dashed line in Fig. 2b). With increasing target concentration, the amounts of PA and RA will increase based on eqn (2a) and (2b). S_T increases to a peak value with the increasing target concentration when the concentration is above the detection limit, mainly because the increased amount of PA conjugates is easily captured by R to form the sandwich type of RPA in the test line. However, we observed a decrease in signal intensity with further increase of target concentration because the increased amount of RA will block the immobilization of PA conjugates in the test line. Alternatively, the increased $C_{P\text{-}in}$ can produce an amplified intensity S_T. This can be attributed to the increased $C_{P\text{-}in}$, which will produce more complex PA that can be easily captured in the test line.

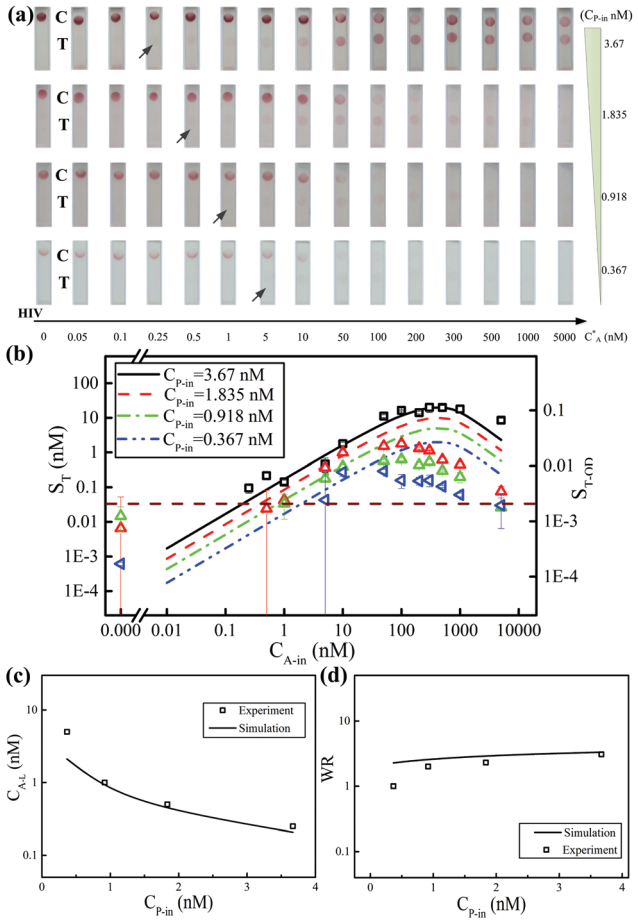

Fig. 2 Relationship between the reporter particle concentration and the performance of LFAs in nucleic acid HIV detection. (a) Experimental results applying different reporter particle concentrations; (b) comparison between the experimental data and simulation result under different reporter particle concentrations; (c) comparison of detection limits from the experiment and simulation; (d) comparison of WR from the experiment and simulation.

For further comparison of LFA performance, we extracted detection limits $C_{A\text{-}L}$ and working range WR from the experimental and simulation results (Fig. 2b). Thus, the experimental detection limits are found to be 5, 1, 0.5, and 0.25 nM, and the simulation detection limits are 2.11, 0.83, 0.41, and 0.21 nM, respectively. The $C_{A\text{-}L}$ in the simulation and experiment shows a decreasing tendency with the increase in $C_{P\text{-}in}$ (Fig. 2c), which indicates that a high $C_{P\text{-}in}$ would produce a high sensitivity of LFAs. However, this decreasing trend gradually becomes mild possibly due to the limited capture capacity of fixed C_{R0}. In addition, the WR is widened by the increase in $C_{P\text{-}in}$, as reflected by the simulation and experiment results (Fig. 2d). However, the slope of this curve gradually becomes small, which indicates that an appropriately high $C_{P\text{-}in}$ is beneficial for improving the linear work range. We can use this model to predict the $C_{A\text{-}L}$ and WR under different $C_{P\text{-}in}$ by comparing with a determined experimental detection limit for designing an optimized LFA.

We also compared the simulated signal intensity in the control line (S_C) with the experimental results $S_{C\text{-}OD}$ (Fig. 3). The signal intensities in the simulation and experiment present a reasonable match, which further validates our model. We found that S_C in the control line remains stable when the target concentration is below 100 nM. This is mainly due to the excess free reporter particles, which play dominant roles in forming complex PA below a certain target concentration. The S_C sharply decreases when the increased target concentration is above 100 nM mainly because the inadequate free reporter particles are blocked by the excess target to form the complex PA. At a fixed $C_{P\text{-}in}$, the signal intensity in the control line decreases with the decrease in reporter particle

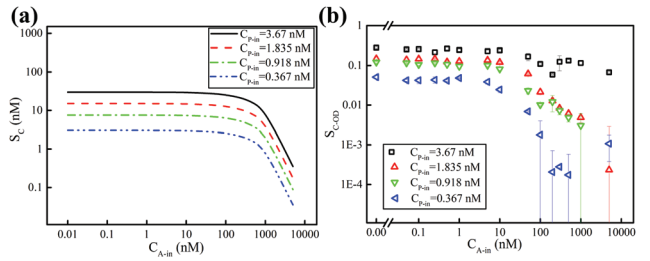

Fig. 3 Relationship between the signal intensity in the control line and the reporter particle concentration. (a) Simulation results; (b) experimental result extracted from Fig. 2a.

concentration due to the limited free reporter particle for the control probe.

3.2 Performance of LFAs with different initial capture probe concentrations

Since the initial capture probe concentration is also a vital parameter in preparing LFA strips, we performed both experiments and simulations to investigate its effects on the performance of LFAs (Fig. 4). From the experimental images in Fig. 4a, we observed that, for all four different C_{R0} (*i.e.* 123.7, 309.3, 618.5, and 1237 nM), the detection signals in the test line increase and then decrease with increasing concentrations of target HIV in the range of $C_{A\text{-}in}$ = 0–5000 nM (*i.e.*, Hook effect phenomenon). At a fixed $C_{A\text{-}in}$, the signal intensity in the test line increases with the increase in C_{R0}.

To understand these observations, we performed mathematical simulations by using varying C_{R0}, (*i.e.*, 123.7, 309.3, 618.5, and 1237 nM) to detect a series of $C_{A\text{-}in}$. We also observed that the variations of S_T in the test line with the increase in target analyte for different C_{R0} are in accordance with the experimental observations (Fig. 4b). At a fixed concentration of target HIV, a high C_{R0} produces a strong detection signal in the test line because the test line has a high capability to capture PA conjugates and free target A. Similar to Fig. 2b, the threshold value for the visible detection signal ($S_{T\text{-}L}$ = 0.03 nM) is also applied to distinguish the visible and invisible signal regions in simulation.

Furthermore, we extracted the detection limit $C_{A\text{-}L}$ and WR from Fig. 4b. Correspondingly, the experimental detection limits are found to be 50, 10, 5, and 0.25 nM, and the simulation detection limits are 1.86, 0.73, 0.38, and 0.20 nM based on the threshold value for different C_{R0}. The detection limits $C_{A\text{-}L}$ in the simulation and experiment decreased significantly with the increase in C_{R0} (Fig. 4c). This is mainly because numerous capture probes in the test line have a strong capacity to capture the target analytes. However, this decreasing phenomenon gradually becomes insensitive with the increase in C_{R0} because the limited sample volume (80 μL) and reaction time (600 s) in the detection of nucleic acid HIV resulted in an inadequate RPA accumulation (*i.e.*, visible signal). The variation of detection limits under different C_{R0} is more obvious than that of varying $C_{P\text{-}in}$. Our simulation results have some

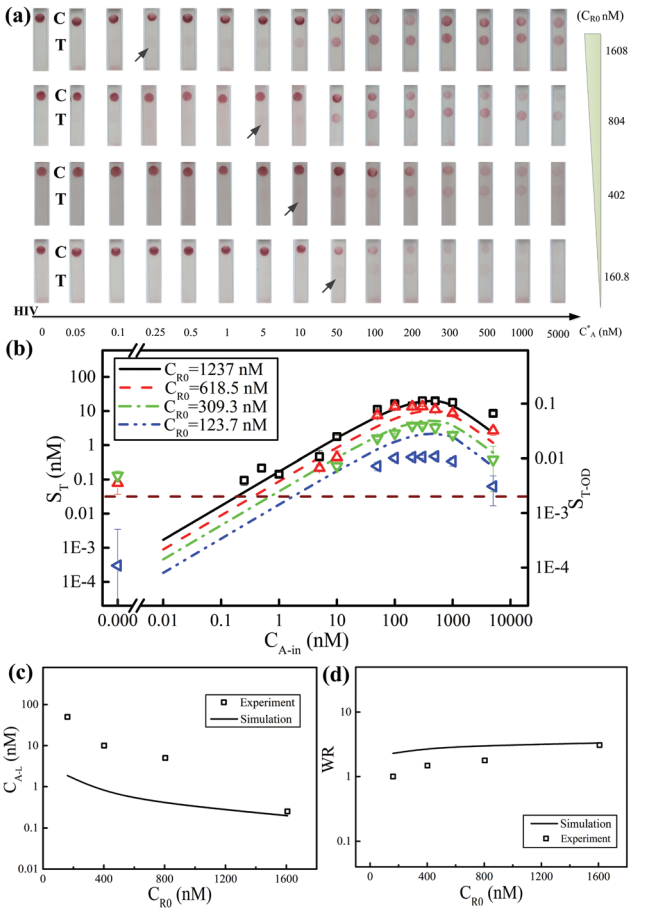

Fig. 4 Relationship between the capture probe concentration and the performance of LFAs. (a) Experimental results applying different capture probe concentrations; (b) comparison between the experimental data and simulation result with varying capture probe concentrations; (c) comparison of the detection limit from the experiment and simulation; (d) comparison of WR from the experiment and simulation.

slight deviations from the experimental $C_{A\text{-}L}$. This is mainly because the signal intensities corresponding to each experimental detection limit at different target concentrations are not completely consistent, resulting in a qualitatively determined threshold value (Fig. 2b). And this threshold value probably makes a difference in choosing the detection limits in Fig. 4b. In addition, WR in the simulation and experiment presents an amplified tendency with the increase in capture probe concentration (Fig. 4d). Therefore, C_{R0} should be increased to achieve a wide linear WR and semi-quantitative detection. Similarly, the mathematical model can be used to predict the detection limit and WR in optimizing the performance of LFA by comparing with a determined experimental detection limit.

Correspondingly, we observed a similar tendency of signal intensity in the control line (S_C) by comparing the simulation result with the experiment data (Fig. 5). S_C remains stable when the target concentration is below 200 nM and then decreases with the further increase in target analyte concen-

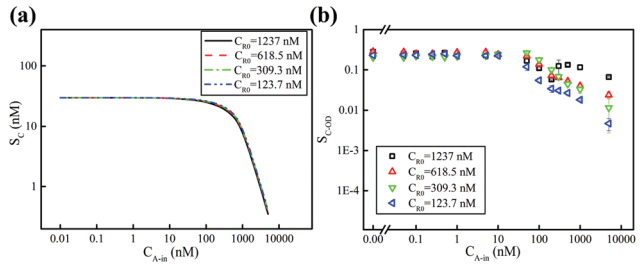

Fig. 5 Relationship between the signal intensity in the control line and capture probe concentration. (a) Simulation results; (b) experimental result extracted from Fig. 4a.

tration. However, S_C is not sensitive with a varying C_{R0} due to the amount of reporter particles, which is the main influence factor for S_C based on eqn (2e), and remains constant in the LFA strip preparation. This agreement provides further validation for our mathematical model.

3.3 Performance of LFAs with various association rate constants

The association rate constant k_a plays a significant role in the performance of LFAs. However, few efforts have been made in investigating the effects of the association rate constant on the performance of LFAs. Experimental studies require a considerable amount of efforts in selecting appropriate nucleic acid sequences with different k_a values because different k_a values correspond to different reagent reactions in various LFA detection processes. Therefore, we can use the simulation method to analyze the influences of k_a under different nucleic acid reactions (Fig. 6). From Fig. 6a, we observed the Hook effect

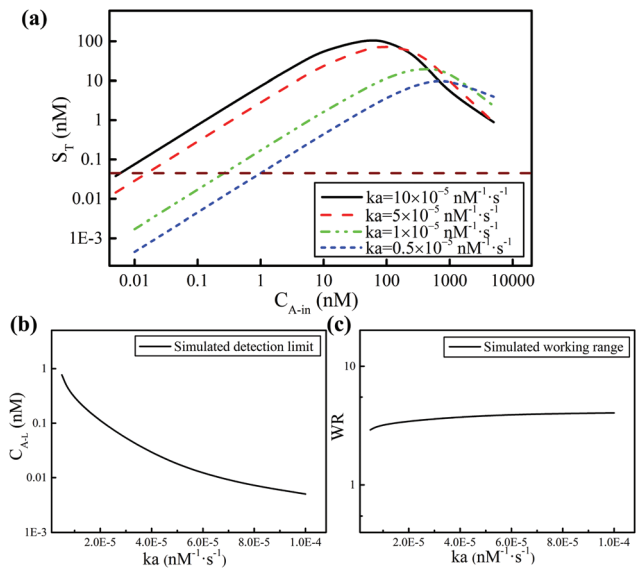

Fig. 6 Performance optimization of LFA with various association rate constants. (a) Hook effect phenomenon at various association rate constants; (b) detection limit as a function of k_a; (c) working range as a function of k_a.

phenomenon for different association rate constants (*i.e.*, k_a = 0.5 × 10^{-5}, 1 × 10^{-5}, 5 × 10^{-5}, and 10 × 10^{-5} nM^{-1} s^{-1}). At a fixed target HIV concentration, a great association rate constant k_a will obviously produce a strong S_T in the test line according to the high reaction efficiency of reagents. The threshold value ($S_{T\text{-}L}$ = 0.03 nM) was also used to extract the detection limit $C_{A\text{-}L}$ and the WR from Fig. 6a in the following analysis.

With the same method, the simulation detection limits $C_{A\text{-}L}$ of four k_a are extracted as 0.771, 0.208, 0.012, and 0.005 nM from Fig. 6a. The detection limits significantly decrease with increasing association rate constant (Fig. 6b). This is mainly due to that a high k_a will improve the reagents' reaction efficiency, resulting in a high capture efficiency of capture probes in the test line. Additionally, WR gradually increases with an increase in association rate constant, mainly due to the high reaction efficiency and strong capture capacity of capture probes. These phenomena indicate that we can select a reasonable target nucleic acid sequence with a high association rate constant from the target DNA sequence and we can also increase the ionic strength at salt concentrations to increase the association rate constant and to optimize the performance of LFAs.

As abovementioned discussions, our mathematical model provides a powerful method to semi-quantitatively analyze the LFA performances under various design parameters (*i.e.*, inlet reporter particle concentration, initial capture probe concentration, and association rate constant). This CDR LFA model is also appropriate to analyze the working process in LFAs with an antigen–antibody reaction, according to the same working principles of sandwich format LFAs based on the nucleic acid reaction or antigen–antibody reaction.[16,32] Once the conversion method for the LFA design parameters between the simulation and experiment is established, (specially k_a can be obtained by protein–protein interaction theory[33]), the CRD model also can provide a semi-quantitative analysis for LFA based on the antigen–antibody reaction. Apart from its advantages, the presented model still suffers from some limitations in providing comprehensive prediction of the LFA performance. For instance, as the model only considers the NC membrane as the main calculation domain, it neglects the complex porous structures of sample and absorption pads, which may have an effect on the reagents' reaction. The model is also short in analyzing the effects of the distribution of the capture probe in the test line on the LFA performance. Based on these defects, we can make reasonable modifications to achieve these functions in the following study.

4. Conclusion

In this paper, we developed a mathematical model to quantitatively analyze the effects of the detection limit and working range on LFAs. Our simulation results are verified by direct comparison with our experimental signals in the test and control lines. Based on the lowest experimental detection

limit, the threshold value is determined to be 0.03 nM. Then, we used this threshold value to evaluate the detection limits in our simulation results. A high concentration of the inlet reporter particles or initial capture probe in the preparation of LFA strips will produce high sensitivity and a wide working range. Alternatively, the variation trend of detection limits under different initial capture probe concentrations is more obvious than the variation trend under different inlet reporter particle concentrations. By comparing an experimental detection limit, the developed model can be extended to predict the detection limit and working range in designing an LFA device under different concentrations of inlet reporter particles, initial capture probe, and association rate constants. LFA detection should be optimized to select a reasonable target nucleic acid sequence with a high association rate constant. These fundamental investigations can provide suggestions for the design and optimization of LFAs.

Conflicts of interest

There are no conflicts to declare.

Acknowledgements

This work was financially sponsored by the National Natural Science Foundation of China (51322604), the National Program for Support of Top-Notch Young Professionals, the Foundation for Innovative Research Groups of the National Natural Science Foundation of China (No. 51322604), the National Instrumentation Program of China (2013YQ190467), the Key Program for Science and Technology Innovative Research Team in Shaanxi Province of China (2017KCT-22), the Program for Innovative Research Team in Yulin Shaanxi Province of China (2017KJJH-02), the China Postdoctoral Science Foundation (2017M623167) and the Initiative Postdocs Supporting Program (BX201700186).

References

1 A. K. Yetisen, M. S. Akram and C. R. Lowe, *Lab Chip*, 2013, **13**, 2210–2251.
2 X. Ge, A. M. Asiri, D. Du, W. Wen, S. Wang and Y. Lin, *TrAC, Trends Anal. Chem.*, 2014, **58**, 31–39.
3 J. Hu, S. Wang, L. Wang, F. Li, B. Pingguan-Murphy, T. J. Lu and F. Xu, *Biosens. Bioelectron.*, 2014, **54**, 585–597.
4 Z. Liu, J. Hu, Y. Zhao, Z. Qu and F. Xu, *Appl. Therm. Eng.*, 2015, **88**, 280–287.
5 J. R. Choi, Z. Liu, J. Hu, R. Tang, Y. Gong, S. Feng, H. Ren, T. Wen, H. Yang, Z. Qu, B. Pingguan-Murphy and F. Xu, *Anal. Chem.*, 2016, **88**, 6254–6264.
6 Z. Liu, J. Hu, Z. Qu and F. Xu, in *Handbook of Immunoassay Technologies*, ed. S. K. Vashist and J. H. T. Luong, Academic Press, London, 2018, ch. 8, pp. 183–201.
7 S. K. Vashist, A. G. Venkatesh, E. Marion Schneider, C. Beaudoin, P. B. Luppa and J. H. T. Luong, *Biotechnol. Adv.*, 2016, **34**, 272–290.
8 C. Parolo, M. Medina-Sánchez, A. de la Escosura-Muñiz and A. Merkoçi, *Lab Chip*, 2013, **13**, 386–390.
9 J. R. Choi, J. Hu, Y. Gong, S. Feng, W. A. B. Wan Abas, B. Pingguan-Murphy and F. Xu, *Analyst*, 2016, **141**, 2930–2939.
10 Q. Fang, L. Wang, Q. Cheng, J. Cai, Y. Wang, M. Yang, X. Hua and F. Liu, *Anal. Chim. Acta*, 2015, **881**, 82–89.
11 Y. K. Oh, H.-A. Joung, H. S. Han, H.-J. Suk and M.-G. Kim, *Biosens. Bioelectron.*, 2014, **61**, 285–289.
12 P. L. A. M. Corstjens, M. Zuiderwijk, M. Nilsson, H. Feindt, R. Sam Niedbala and H. J. Tanke, *Anal. Biochem.*, 2003, **312**, 191–200.
13 M. Sajid, A.-N. Kawde and M. Daud, *J. Saudi Chem. Soc.*, 2015, **19**, 689–705.
14 H.-Y. Yin, P.-T. Chu, W.-C. Tsai and H.-W. Wen, *Food Chem.*, 2016, **192**, 934–942.
15 S. Qian and H. H. Bau, *Anal. Biochem.*, 2004, **326**, 211–224.
16 S. Qian and H. H. Bau, *Anal. Biochem.*, 2003, **322**, 89–98.
17 M. S. Ragavendar and C. M. Anmol, *presented in part at the Engineering in Medicine and Biology Society (EMBC), 2012 Annual International Conference of the IEEE*, San Diego, CA, USA, Aug. 28-Sept. 1, 2012.
18 Z. Liu, J. Hu, A. Li, S. Feng, Z. Qu and F. Xu, *Sens. Actuators, B*, 2017, **248**, 699–707.
19 N. Zeng, Z. Wang, Y. Li, M. Du and X. Liu, *IEEE Trans. Biomed. Eng.*, 2011, **58**, 1959–1966.
20 N. Zeng, Z. Wang, Y. Li, M. Du and X. Liu, *IEEE Trans. Nanotechnol.*, 2012, **11**, 321–327.
21 J. R. Choi, J. Hu, S. Feng, W. A. B. Wan Abas, B. Pingguan-Murphy and F. Xu, *Biosens. Bioelectron.*, 2016, **79**, 98–107.
22 R. Tang, H. Yang, J. R. Choi, Y. Gong, J. Hu, S. Feng, B. Pingguan-Murphy, Q. Mei and F. Xu, *Talanta*, 2016, **152**, 269–276.
23 J. Shang and X. Gao, *Chem. Soc. Rev.*, 2014, **43**, 7267–7278.
24 J. Hu, L. Wang, F. Li, Y. L. Han, M. Lin, T. J. Lu and F. Xu, *Lab Chip*, 2013, **13**, 4352–4357.
25 J. G. Wetmur, *Annu. Rev. Biophys. Bioeng.*, 1976, **5**, 337–361.
26 J. G. Wetmur and J. Fresco, *Crit. Rev. Biochem. Mol. Biol.*, 1991, **26**, 227–259.
27 V. Shkolnikov and J. G. Santiago, *Anal. Chem.*, 2014, **86**, 6229–6236.
28 J. McGrath, M. Jimenez and H. Bridle, *Lab Chip*, 2014, **14**, 4139–4158.
29 A. W. Peterson, R. J. Heaton and R. M. Georgiadis, *Nucleic Acids Res.*, 2001, **29**, 5163–5168.
30 X. L. Wang, T. Tsuru, M. Togoh, S. I. Nakao and S. Kimura, *J. Chem. Eng. Jpn.*, 1995, **28**, 372–380.
31 Z. G. Qu, W. Q. Li, J. J. Zhang and W. Q. Tao, *Numer. Heat Transfer, Part A*, 2015, **67**, 189–209.
32 D. V. Sotnikov, A. V. Zherdev and B. B. Dzantiev, *Anal. Chem.*, 2017, **89**, 4419–4427.
33 M. Schlosshauer and D. Baker, *Protein Sci.*, 2004, **13**, 1660–1669.